A Crystalline 2D Fullerene-Based Metal Halide Semiconductor for Efficient and Stable Ideal-bandgap Perovskite Solar Cells

Weicheng Shen, Ali Azmy, Guang Li, Anamika Mishra, Zois Syrgiannis, Wenwen Zheng, George Volonakis, Mikaël Kepenekian, Jacky Even, Lukasz Wojtas, et al.

To cite this version:

Weicheng Shen, Ali Azmy, Guang Li, Anamika Mishra, Zois Syrgiannis, et al.. A Crystalline 2D Fullerene-Based Metal Halide Semiconductor for Efficient and Stable Ideal-bandgap Perovskite Solar Cells. Advanced Energy Materials, 2024, 14 (23), pp.2400582. 10.1002/aenm.202400582. hal-04564542

HAL Id: hal-04564542
https://hal.science/hal-04564542v1

Submitted on 1 Jul 2024

A Crystalline 2D Fullerene-based Metal Halide Semiconductor for Efficient and Stable Ideal-bandgap Perovskite Solar Cells

Weicheng Shen,[1,6#] Ali Azmy,[2,#] Guang Li,[1,6#] Anamika Mishra,[2] Zois Syrgiannis,[3] Wenwen Zheng,[1,*] George Volonakis,[4] Mikaël Kepenekian,[4] Jacky Even,[5] Lukasz Wojtas,[2] Cheng Wang,[6] Lishuai Huang,[6] Weiqing Chen,[6] Shun Zhou,[6] Jin Zhou,[6] Guojun Zeng,[6] Dexin Pu,[6] Hongling Guan,[6] Guojia Fang,[6] Weijun Ke,[6] and Ioannis Spanopoulos[2,*]

[1]*Hubei Key Laboratory of Optical Information and Pattern Recognition, School of Optical Information and Energy Engineering, Wuhan Institute of Technology, Wuhan 430205, China*

[2]*Department of Chemistry, University of South Florida, Tampa, FL, 33620, USA*

[3]*Nanoneurosciences LLC, 16192 Coastal HWY, Lewes, De, 19958, USA*

[4]*Univ Rennes, ENSCR, CNRS, ISCR-UMR 6226, F-35000 Rennes, France*

[5]*Univ Rennes, INSA Rennes, CNRS, Institut FOTON-UMR6082, F-35000 Rennes, France*

[6]*Key Lab of Artificial Micro- and Nano-Structures of Ministry of Education, School of Physics and Technology, Wuhan University, Wuhan 430072, China*

Abstract

Despite advances in mixed tin-lead (Sn-Pb) perovskite-based solar cells, achieving both high- efficiency and long-term device stability remains a major challenge. Current device deficiencies stem partly from inefficient carrier transport, originating from defects and improper band energy alignment among the device's interfaces. Developing multifunctional interlayer materials simultaneously addressing the above concerns poses an excellent strategy. Herein, through molecular and crystal engineering, we synthesized an amine-functionalized C_{60} mono-adduct derivative (C_{60}-2NH_3 = bis(2-aminoethyl) malonate-C_{60}) is utilized for the synthesis of the first crystalline fullerene-based 2D metal halide semiconductor, namely (C_{60}-2NH_3)Pb_2I_6. Single crystal XRD studies elucidated the structure of the new material, while DFT calculations highlighted the strong contribution of C_{60}-2NH_3 to the electronic density of states of the conduction band of (C_{60}-2NH_3)Pb_2I_6. Utilization of C_{60}-2NH_3 as an interlayer between a $FA_{0.6}MA_{0.4}Pb_{0.7}Sn_{0.3}I_3$ perovskite and a C_{60} layer offered superior band energy alignment, reduced non-radiative recombination, and enhanced carrier mobility. The corresponding perovskite solar cell (PSC) device achieved a PCE value of 21.64%, maintaining 90% of its initial efficiency, after being stored under an N_2 atmosphere for 2400 h. Our work sets the foundation for developing a new family of functional materials, namely Fullerene Metal Halide Semiconductors (FMHS), targeting applications from photovoltaics to catalysis, transistors, and supercapacitors.

Keywords: Band energy alignment, charge transfer, fullerene-based semiconductors, ideal-bandgap, multifunctional interfaces, perovskite solar cells

1. Introduction.

Perovskite solar cells (PSCs) pose as a next-generation photovoltaic technology with immense potential for commercialization.[1] The heart of the device is an organic-inorganic (hybrid) perovskite semiconductor serving as the light-absorbing layer, which bears an unparallel combination of attributes, such as fine tunable optical, mechanical and electronic properties,[2] low-cost solution processability,[3] long carrier lifetimes[4] and diffusion lengths,[5] and high light absorption coefficients.[6] By means of material and device engineering, the maximum power conversion efficiency (PCE) of single-junction PSCs using ~1.55 eV-bandgap light absorbers grew from 3.8% to 26.1% in almost 15 years.[7] Despite the impressive PCE values, limitations still hinder device performance from reaching the theoretical efficiency values of ~30%.[8]

The presence of multiple interfaces within a solar cell device, consisting of the electron transporting layer (ETL), light absorbing layer, hole transporting layer (HTL), and of course the electrodes, increases the system complexity and promotes the presence of traps and defects. The latter can impact band edge energy alignment among the layers and hinder carrier transport.[9] In particular, 2,2′,7,7′-Tetra-kis(*N*, *N*-di-*p*-methoxyphenyl-amine)9,9′-spirobifluorene which is the most common HTL material in n-i-p PSCs, features issues pertaining to its low hole mobility,[10] poor conductivity,[11] thermal instability,[12] significant voltage losses,[13] and poor adhesion on the perovskite surface.[14] Similarly, fullerene (C_{60}) or [6,6]-phenyl-C_{61}-butyric acid methyl ester (PCBM) serving as ETL, demonstrate disadvantages such as aggregation at the interfaces,[15] and dimerization issues under light illumination that hinder charge transport.[16]

Towards addressing the above concerns, utilization of novel, functionalized HTLs or ETLs has proven to alleviate the aforementioned issues, offering at the same time high PCE values and long-term environmental stability.[17] Of particular interest is the use of custom-made fullerene-based molecules, e.g., PCBM, serving either as the ETL in the most inverted (p-i-n) PSCs or as interlayers among the light-absorbing layer and the ETL. In this regard, Li et al. reported that by adding a fullerene derivative, fullerene-n-butyl-pyridine (C_{60}-BPy) among the perovskite layer and the ETL, the C_{60}-BPy can be anchored to the perovskite surface through coordination, modulate the interfacial energy level arrangement, and increase the carrier transport capacity.[18] Zhou et al. developed an amino-functionalized fullerene derivative (C_{60}-BPAM) incorporated into a 2D/3D hybrid perovskite solar cell, leading to an increase in the electron density in the 2D/3D perovskite thus inducing an additional built-in electric field that facilitates electron transfer in PSCs.[19] Xing et al. assembled corannulene and C_{60} into a smooth and compact film by a strategy that retards and inhibits the spontaneous aggregation of C_{60} and enhances electron transport.[20] You et al. introduced a phosphonate acid-functionalized fullerene derivative as a grain-boundary modulator in hybrid cationic perovskite to consolidate the crystal structure, which improves the film's tolerance to light, heat, and moisture.[21] Fakharuddin et al., synthesized a triethylleneglycol C_{60} mono-adduct derivative (termed as EPF03) and tested it as a novel electron transport material to replace PCBM in inverted PSCs. They found that PSC enhanced performance derived from improved electron extraction and reduced recombination.[22] Sun et al. utilized a series of regio-isomers (trans-2, trans-3, trans-4) of diethylmalonate-C60 bis-adduct (DCBA) as ETLs. Their utilization gave rise to a shallower-lying conduction band position, favorable molecular packing, and enhanced interfacial interaction.[23] Jiang et al. assembled a series of fullerene dyads FP-Cn (n = 4, 8, 12) to replace PCBM as an electron transport layer, where fullerene is linked with a terpyridine chelating group via a flexible alkyl chain of different lengths as a spacer. Corresponding devices recorded a PCE value of 21.69%, higher than that of PCBM/C60 (20.09%), benefiting from improved electron extraction and transport as well as reduced charge recombination loss.[24] Yin et al. developed a new type of ETM by polymerizing C_{60} fullerene with an aromantic linker unit. The resultant polyfullerene (PFBS-C12) maintained the unique optoelectronic properties of fullerene molecules and addressed the aforementioned aggregation problem of C_{60} and PCBM.[25]

Despite the plethora of functionalized C_{60} molecules and their undoubtful positive impact on device performance, there is a lack of direct structural evidence at the interface between the perovskite layer and the ETL, that can consolidate the affinity and the interaction among the two layers. To address this severe deficiency, we utilized molecular and crystal engineering to design and synthesize a crystalline fullerene-based 2D metal halide semiconductor, namely $(C_{60}\text{-}2NH_3)Pb_2I_6$, ($C_{60}\text{-}2NH_3$ = bis(2-aminoethyl) malonate-C_{60}). To the best of our knowledge, this is the first time a crystalline 2D fullerene-based metal halide semiconductor has been reported in single-crystal form.[26] In terms of material engineering, the presence of the ammonium functional groups would allow $C_{60}\text{-}2NH_3$ to serve as a counter cation to a perovskite/metal halide compound. Interestingly, the large size of the fullerene molecule was considered by many “improbable” to template a proper 2D perovskite network. This is true since adjacent organic counter-cations in a proper Ruddlesden-Popper (RP) perovskite lay at a distance of ~4 Å for the bulkiest perylene-o-ethylammonium based $(C_{20}H_{20}ON)_2PbI_4$ 2D perovskite,[27] much smaller than the 7 Å diameter of C_{60}.[28] Apparently, in the case of $(C_{60}\text{-}2NH_3)Pb_2I_6$, the system overcomes this obstacle by changing the connectivity of the $[PbI_6]^{4-}$ octahedra from fully corner-sharing (for an RP perovskite) to corner and edge-sharing octahedra, thus creating in plane voids. In return, this configuration allows the accommodation of the bulkier $C_{60}\text{-}2NH_3$ among the 2D layers of the metal halide material (a proper halide perovskite must consist of corner-sharing octahedra only, similar to oxide perovskites).[29] Single crystal and powder XRD studies elucidated the structure of the new material. Density functional theory (DFT) studies shed light on its electronic properties, revealing a type-II band alignment between the organic and inorganic sublayers in sharp contrast to current reported 2D RP and DJ perovskites.[30]. The corresponding compound, due to its hybrid nature, is expected to have a strong affinity with both the perovskite layer and the C_{60} layer through electrostatic and π-π interactions respectively, thus facilitating carrier transport across layers. To test our hypothesis on its potential in PSCs we utilized $(C_{60}\text{-}2NH_3)$ as an interlayer film between a perovskite layer with a composition of $FA_{0.6}MA_{0.4}Pb_{0.7}Sn_{0.3}I_3$ and the C_{60} layer. It was demonstrated that the $C_{60}\text{-}2NH_3$-modified perovskite films exhibited superior energy level arrangement at the interface, which significantly suppressed non-radiative recombination and enhanced carrier transport. Based on this design, we obtained a 21.64% PCE value for mix Sn-Pb 1.34 eV-ideal-bandgap PSCs. Notably, our $C_{60}\text{-}2NH_3$-modified devices realized enhanced long-term stability by retaining 90% of their original efficiency after 2400 h of storage under a nitrogen atmosphere, coupled with enhanced air and moisture stability. Our work sets the foundation for the development of a new family of functional materials, namely Fullerene Metal Halide Semiconductors (FMHS), which can be utilized for applications beyond photovoltaics, to catalysis,[31] transistors,[32] and supercapacitors.[33]

2. Results and Discussion

2.1. Synthesis and Characterization of the Amino-Functionalized Fullerene Derivative and Metal Halide Material

The amino-functionalized fullerene derivative (abbreviated as C_{60}-$2NH_3I_2$) was synthesized facilely via a three-step reaction as an iodide salt. As shown in Scheme S1 (Supporting Information), the first step is the synthesis of the functionalized malonate ester. It was acquired based on a previously reported procedure by treatment of 2.2 eq of *tert*-butyl *N*-(2-hydroxyethyl) carbamate in dry methylene chloride with 1 eq of malonyl chloride and 1.5 eq of pyridine (Figures S1-S3, Supporting Information).[34] The second step is a Bingel-Hirsch reaction to synthesize the fullerene-malonate monoadduct (Scheme S2, Figures S4 and S5, Supporting Information).[35] To that end, 1eq of C_{60}, 1.5 eq CBr_4, 1.5 eq malonate, and 3 eq of DBU were mixed at 0 °C. The reaction is completed after 2 h. The monoadduct is collected after purification with column chromatography and characterized with NMR and mass spectrometry (see Supporting Information). Finally, the carbamate-protecting groups on monoadduct were removed using hydriodic acid in methylene chloride to generate C_{60}-$2NH_3I_2$ (Scheme S3, Figures S6 and S7, Supporting Information).

For the material synthesis, we used the anti-solvent method to acquire single crystals of $(C_{60}\text{-}2NH_3)Pb_2I_{6.}$ The ligand iodide salt (C_{60}-$2NH_3I_2$) and PbI_2 were dissolved in dimethyl formamide (DMF) and this reaction vial was added inside a larger vial containing dichloromethane (CH_2Cl_2) as the antisolvent. Slow diffusion of CH_2Cl_2 gave rise to dark orange crystals, which are very sensitive to being isolated due to the volatility of the antisolvent. Fast solvent diffusion can dissolve the crystals instantly upon drying.

Single crystal X-ray diffraction (XRD) studies revealed a 2D layered structure that crystallizes in the triclinic space group *P*-1 (Figure 1; Table S1, Supporting Information). The structure consists of single inorganic layers of corner and edge-sharing $[PbI_6]^{4-}$ octahedra that are separated and charged balanced by a double organic layer of opposite facing C_{60}-$2NH_3$. Evidently, the inorganic layers are eclipsed along the *c*-axis, laying at a distance of ~20 Å. There are two crystallographically independent Pb atoms and six I atoms forming a tetramer of edge-sharing octahedra that propagates in-plane by sharing corners with adjacent tetramers (Figure 1).

Corresponding Pb(1)-I and Pb(2)-I bond lengths span from 3.011(3) Å to 3.320(2) Å, and 3.128(3) Å to 3.311(3) Å respectively (Table S4, Supporting Information), while similar variation is observed for the I-Pb-I angles that range from 84.04(6)° to 174.31(7)° for the cis and trans arrangements respectively (Table S5, Supporting Information). This small degree of octahedral distortion is ascribed to the presence of multiple moderate hydrogen bonds, ranging from 2.3 Å to 3 Å, among the hydrogen atoms of the ammonium (R-NH_3) and the methylene (-CH_2-) groups of the organic counter-cations and the iodide atoms of the inorganic octahedra (Figure S8, Supporting Information).

Moreover, octahedral distortion can be further quantitatively evaluated by the calculated bond length distortion (Δd), $\Delta d = \frac{1}{6}\sum_{i=1}^{6}\left(\frac{di^2 - d_0^2}{d_0^2}\right)$, ($d_i$ are the six Pb−I bond lengths and d_0 is the mean Pb−I bond length within an octahedron), and bond angle variance (σ^2), $\sigma^2 = \frac{1}{11}\sum_{i=1}^{12}(\theta_i - 90°)^2$, ($\theta_i$ are the 12 I−Pb−I bond angles within an octahedron).[36] The observed Δd values of 0.03 and 0.02 for the $[Pb(1)I_6]^{4-}$ and $[Pb(2)I_6]^{4-}$ respectively, as well as the σ^2 values of 16.4 deg.^{2} and 21.6 deg.^{2} for the $[Pb(1)I_6]^{4-}$ and $[Pb(2)I_6]^{4-}$ respectively, reveal a higher degree of distortion for the $(C_{60}\text{-}2NH_3)Pb_2I_6$ over conventional n=1 2D perovskites, such as $(C_5H_{11}NH_3)_2PbI_4$ (σ^2 = 5.7 deg.^{2}),[37] $(C_{12}H_{25}NH_3)_2PbI_4$ (σ^2 = 5.9 deg.^{2})[38] and (perylene-*O*-ethyl-NH_3)$_2PbI_4$ (σ^2 = 3.5 deg.^{2}).[27]

Examining closer the organic part of the structure, C_{60}-2NH_3 counter-cations feature an anti-configuration on each of the organic sublayers, they are eclipsed in-plane, while they are staggered out-of-plane (along the *c* stacking axis). Each C_{60}-2NH_3 has four nearest neighbors in-plane, therefore its packing configuration resembles the packing of a C_{60} solid, which consists of an *fcc* lattice of C_{60} molecules.[39] Adjacent C_{60}-2NH_3 lay at a distance of 3.2 Å in-plane, and at 3.7 Å out-of-plane, indicative of the extensive π-π interactions among the C_{60}-2NH_3 molecules (Figure 2a-c). These values are consistent with the packing distances of crystalline C_{60} (~3.1 Å) and the stacking values of graphene layers in graphite (3.35 Å).[40]

In-house powder X-ray diffraction studies (PXRD) verified the uniform phase purity of the corresponding material, as the experimental and calculated patterns from single crystal XRD studies are identical (Figure S9, Supporting Information).

2.2 DFT studies

We used calculations based on density functional theory (DFT, see Supporting Information) to investigate the electronic and optical properties of $(C_{60}\text{-}2NH_3)Pb_2I_6$. The band structure of the compound, shown in Figure 2d, shares common features with layered halide perovskites (i.e., with corner-sharing octahedra), such as the absence of dispersion in the stacking direction and the fact that the valence band maximum (VBM) is consisting of Pb s-orbitals and I p-orbitals (Figure 2d; Figure S10, Supporting Information).[41] The electronic states of the organic cation are found ca. 0.2 eV below the VBM (Figure S11, Supporting Information), where there is no orbital overlap between the $[Pb_2I_6]^{2-}$ and $[C_{60}\text{-}2NH_3]^{2+}$ moieties. However, in sharp contrast with prototypical layered halide perovskites, the conduction band minimum (CBM) does not involve the expected Pb p-orbitals but cation states (Figures 2d, S10 and S11, Supporting Information), leading to an indirect band gap from V to X, which is calculated at 1.48 eV with HSE06 hybrid functional corrections (see Supporting Information).

Similarly to layered halide perovskites, we propose to consider $(C_{60}\text{-}2NH_3)Pb_2I_6$ as a composite material resulting from inorganic and organic substructures.[42] In most perovskites, the low-bandgap inorganic layer combines with the large-bandgap organic layer to form a type-I quantum well, where charge carriers are confined to the inorganic network. Here, we can define the two neutral subsystems as $Cs_2Pb_2I_6$ and $C_{60}\text{-}2CH_3$ for the inorganic and organic layers, respectively (see Supporting Information). The inorganic layer (Figure 2e) presents a large direct band gap of 2.45 eV at V, with relatively light in-plane effective masses for holes ($m_{h||}=0.45m_0$) and electron ($m_{e||}=0.12m_0$), given it is a system not-consisting of corner-shared octahedra. In contrast, the organic $C_{60}\text{-}2NH_3$ system (Figure 2f) exhibits a lower band gap of 1.68 eV at X. Therefore, $(C_{60}\text{-}2NH_3)Pb_2I_6$ can be described as a heterostructure with the organic layer as the low-bandgap material, and the inorganic layer as the large-bandgap material. We expect the optical properties of $(C_{60}\text{-}2NH_3)Pb_2I_6$ to be governed by the absorption of

$[C_{60}\text{-}2NH_3]^{2+}$ at lower energy, while the contribution from the inorganic network should be found at higher energy. This is further supported by the computed band gap of 1.68 eV for the organic subsystem, which is in close agreement with the measured absorption threshold using UV-VIS diffuse reflectance studies (1.62 eV, Figure S12, Supporting Information).

In addition, the band structures point to a type-II band alignment with valence states almost aligned between the inorganic and organic substructures (Figure 2g). This configuration plays in favor of the transport of electrons from the inorganic to the organic layer and the C_{60} ETL, a feature that is further supported by a battery of characterization techniques (see next section). In contrast with common layered halide perovskites, the contribution from the highly polarizable $[C_{60}\text{-}2NH_3]^{2+}$ molecules, $\varepsilon_\infty[C_{60}\text{-}2NH_3]=7.1$, is greater than the one of the inorganic network, $\varepsilon_\infty[Pb_2I_6]=4.7$ (Figure 2h). As a result, the dielectric contrast between the organic and inorganic layers is defined by $\frac{\varepsilon_\infty[C60-2NH3]-\varepsilon_\infty[Pb2I6]}{\varepsilon_\infty[C60-2NH3]+\varepsilon_\infty[Pb2I6]} \approx 20\%$ is significantly smaller than for the classical layered halide perovskites ($\approx 40-50\%$ at the same level of theory).[42]

2.3 Solar cell device assembly

To investigate the effect of $C_{60}\text{-}2NH_3$ on the performance of PSCs, we prepared inverted (p-i-n) mixed Sn-Pb ideal bandgap PSCs with a device architecture as shown in Figure 3a. The corresponding device structure was designed as such: Indium tin oxide (ITO)/poly(3,4-ethylenedioxythiophene): poly(styrene sulfonate) (PEDOT: PSS)

/perovskite($FA_{0.6}MA_{0.4}Pb_{0.7}Sn_{0.3}I_3$)/$C_{60}$-$2NH_3$/$C_{60}$/bathocuproine(BCP)/Cu. The presence of a thin layer of (C_{60}-$2NH_3$)Pb_2I_6 can act as a passivating layer improving carrier transport between the 3D perovskite and the ETL. Regarding the passivation mechanism, we hypothesized that (Figure 3b), since there is reduced dielectric confinement of the generated carriers in (C_{60}-$2NH_3$)Pb_2I_6 and the material features high affinity for both the ETL (π-π interactions) and light absorbing layer (electrostatic interactions), its presence would be beneficial for the device performance. In order to validate our hypothesis, we spin-coated a layer of C_{60}-$2NH_3$ on the 3D perovskite films. Corresponding films treated with C_{60}-$2NH_3$ were considered as the target films, while the untreated ones served as the control films.

We first conducted PXRD studies to assess the impact of C_{60}-$2NH_3$ modification on the structural integrity of the films. As depicted in Figure 3c, we observed an increase in the crystallinity of the perovskite layer and the elimination of residual PbI_2 after modification with 0.75 and 5 mg/mL concentrations of C_{60}-$2NH_3$. Additionally, in the PXRD patterns post-processed with 5 mg/mL C_{60}-$2NH_3$, an additional peak emerged near 5°, corresponding to the (002) plane of 2D (C_{60}-$2NH_3$)Pb_2I_6. However, no obvious 2D peaks appeared in the PXRD patterns post-processed with 0.75 mg/mL of C_{60}-$2NH_3$. We speculate that the limited amount of C_{60}-$2NH_3$ on the surface of perovskite films resulted in the formation of an ultra-thin (C_{60}-$2NH_3$)Pb_2I_6 layer. To further assess the ability of C_{60}-$2NH_3$ to suppress PbI_2 segregation and induce the formation of 2D (C_{60}-$2NH_3$)Pb_2I_6 materials, we intentionally introduced excess PbI_2 into the perovskite films and applied a high concentration of C_{60}-$2NH_3$ as post-treatment. As shown in Figure S13 (Supporing Information), the PbI_2 peak is significantly reduced, with two distinct peaks observed at

5.6° and 8.5°, corresponding to the (002) and (003) planes of 2D (C_{60}-$2NH_3$)Pb_2I_6. Corresponding results strongly support the formation of a 2D phase on top of the 3D perovskite after the C_{60}-$2NH_3$ treatment, thus validating the first part of our hypothesis pertaining to the actual formation of a 2D layer.

Following this, we investigated the effect of C_{60}-$2NH_3$ post-treatment on the morphology of perovskite thin films by scanning electron microscopy (SEM), (Figure 3d, e). Evidently, there was some excess PbI_2 at the grain boundaries on the surface of the thin films of the control devices, whereas in the target films which were post-treated with C_{60}-$2NH_3$, PbI_2 carried out the reaction thus decreased, giving rise to smoother perovskite films. This was further corroborated by the previous PXRD studies (Figures S13 and S14, Supporting Information).[43] It is well established that under continuous light and heat, PbI_2 readily decomposes into metallic lead (Pb^0) through the release of iodine (I_2) vapor. These substances tend to produce non-radiative complex centers and promote ion migration, thus accelerating aging and performance degradation of the devices.[44] Therefore, C_{60}-$2NH_3$ post-treatment can enhance PSCs' life to a certain extent. Moreover, the grain sizes of both control and target films were around 750 nm to 800 nm without significant change, as shown in Figure S15 (Supporting Information). Atomic force microscopy (AFM) revealed that the average roughness of the films in the target films decreased from 43.9 nm in the control films to 32.2 nm (Figure S16, Supporting Information), which is attributed to the elimination of PbI_2 on the surface of the films. In return, this behavior favors a uniform coverage of C_{60} on the Sn-Pb perovskite layer after the evaporation of C_{60}, thus reducing the leakage current.[17a, 45]

Apparently, Sn^{2+} in a Sn-Pb perovskite is easily oxidized to Sn^{4+} thus leading to p-type self-doping, and a deep Fermi energy level (E_F), which is detrimental to the performance of PSCs.[46] Ultraviolet photoelectron spectroscopy (UPS) tests were performed to probe the effect of C_{60}-$2NH_3$ post-treatment on the energy levels of the perovskite surfaces (Figure S17, Supporting Information). The secondary electron cutoff energies of these films and the onset of the valence band maxima (E_V) can be used to estimate the energies of E_F and E_V, which, in combination with the optical bandgap of ≈1.34 eV, allowed for the derivation of the conduction band minima (E_C). In Figure 3f the band energy levels of perovskite films treated with and without the introduction of C_{60}-$2NH_3$ are presented. It is evident that compared to the control films, the C_{60}-$2NH_3$ post-treatment was able to bend the energy bands downward, with both E_V and E_C being decreased by 0.15 eV. As a result, this promoted an efficient regulation of the energy level alignment and actually accelerated the electron extraction, thus allowing for a higher efficiency of electron extraction at the interface.[47] Besides, it is interesting to find that although the energy band shifts downward, the E_F moves upward, from -4.6 eV to -4.5 eV, which represents an effective suppression of p-type doping on the surface of the perovskite thin films and a reduction of carrier recombination.[48] In addition, the elevated E_F was further demonstrated with Kelvin probe force microscopy (KPFM) measurements by measuring the surface potentials of the perovskite films with and without C_{60}-$2NH_3$ post-treatment, as shown in Figure 3g, h. It was shown that the average surface potential of the control film was 0.064 V, and that of the target film was -0.015 V. A calibration by highly oriented pyrolytic graphite (HOPG) (Figure S18, Supporting Information) took place and the E_F of the target and control films was calculated to be -4.53 eV and -4.61 eV, respectively (Table S7,, Supporting Information), matching the results obtained by

UPS.

To further investigate the molecular interactions between the perovskite films and C_{60}-$2NH_3$, x-ray photoelectron spectroscopy (XPS) studies were performed, and the results are shown in Figure 3i. We compared the positions of the Pb 4f peaks between those of the control and target films. It was found that the target films' Pb $4f_{7/2}$ peaks were shifted by close to 0.17 eV in the direction of the low binding energy, which indicated that there is some kind of interaction between the C_{60}-$2NH_3$ molecule and the Pb^{2+}, which also was confirmed by the above XRD and SEM results. Secondly, after the introduction of C_{60}-$2NH_3$, as shown in Figure S19 (Supporting Information), the binding energies corresponding to Sn 3d on the surface of perovskite films shifted to lower energy; Sn^{2+} $3d_{5/2}$ decreased from 486.82 eV to 486.44 eV, and Sn^{2+} $3d_{3/2}$ reduced from 495.29 eV to 494.84 eV, so this change of the binding energy implied that there is a strong binding between the perovskite surface ions and C_{60}-$2NH_3$. What's more, a significant decrease in the Sn^{4+} content was observed (Figure S20, Supporting Information), suggesting that C_{60}-$2NH_3$ can suppress the oxidation of Sn^{2+} to Sn^{4+}, thus leading to a decrease in Sn vacancies and a weakening of the p-type self-doping effect.[49]

Shedding light on the effect of C_{60}-$2NH_3$ post-treatment on the optical properties of mixed Sn-Pb ideal-bandgap perovskite films, UV-vis spectroscopy studies were performed. Corresponding absorption spectra of the control and target films, Figure S21 (Supporting Information), showed that there is no significant change in the absorption intensity of the two films. Furthermore, an optical bandgap of about 1.34 eV was obtained by the Tauc plot of Figure S22 (Supporting Information). To further characterize the ultrafast carrier dynamics at the perovskite/C_{60}-$2NH_3$/C_{60} interface, we performed femtosecond transient absorption (fs-TA) tests. C_{60} was evaporated on two of the films, which were more consistent with the device structure. For all four films, the contour plot showed a clear ground state bleaching (GSB) peak at ≈925 nm (Figures S23a-d, Supporting Information). Evidently, the C_{60}-2NH_3-modified film showed a faster GSB peak intensity, indicating a faster rate of charge extraction from the perovskite film to the post-processing layer and then to the neighboring ETL.[50] In addition, according to Figure S24 (Supporting Information), the films with evaporated C_{60} had much weaker GSB peak intensities at the same delay time compared to those without evaporated C_{60}, thus giving rise to extremely fast charge transport. On the contrary, the perovskite/C_{60}-2NH_3/C_{60} thin films exhibit faster GSB peak intensities and relatively shorter photogenerated carrier lifetimes. Both these features strongly suggest that the C_{60}-2NH_3 post-processing can accelerate the extraction and collection of electrons.

Uncovering the effect of C_{60}-2NH_3 on the quality of perovskite films, we evaluated the Urbach energy (E_u) values obtained by external quantum efficiency (EQE) spectra, as shown in Figure S25 (Supporting Information), which decreased from 24.6 meV in the control devices to 15.4 meV after post-treatment with C_{60}-2$NH_{3.}$ Considering that the Urbach energy is a reflection of the energy disorder at the band edges, the decrease in the Urbach energy suggests that C_{60}-2NH_3 leads to less energy disorder at the band edges and a lower density of defective states.[51] To further evaluate the carrier recombination kinetics, we measured the relationship between V_{OC} and J_{SC} and light intensity (p) separately. As shown in Figure 4a, the slope of the curve decreased from 1.36 to 1.20 for the target device. It was regarded that the effect of the Shockley-Reed-Hall complexation on the device performance is weaker when the slope of the curve is close to 1.[52]

Therefore, the introduction of C_{60}-$2NH_3$ reduced the effect of carrier complexation on the device performance and the nonradiative complexation on the perovskite surface. Also, according to Figure S26 (Supporting Information), the slope of the curve for the target device was much closer to 1 than that of the control, indicating that the interfacial recombination was inhibited, thus favoring carrier extraction.[53] To better illustrate this point, electrical impedance spectra (EIS) were recorded to further characterize the carrier complexation behavior of the devices. In Figure 4b, both the target and control devices showed a major semicircle at low frequencies, which was mainly attributed to a complex resistor (R_{rec}) and a constant phase element (CPE). In contrast, the target devices had a larger semicircle, indicating a higher R_{rec} and lower carrier recombination in the device, which facilitated more efficient carrier transport in the devices. Moreover, measurements of the *J*-*V* curves under dark conditions, Figure 4c, revealed that the dark current density of the device post-treated with C_{60}-$2NH_3$ was nearly one order of magnitude lower than that of the control device, which indicates that the target device had fewer grain-boundary defects contributing further to a higher FF.

Taking a step further into identifying the effect of C_{60}-$2NH_3$ modification on the built-in potential (V_{bi}) and carrier extraction of the devices, we performed capacitance-voltage (*C*-*V*) measurements. According to Figure 4d, the Mott-Schottky curve was determined and the V_{bi} of the device was estimated by the following equation:

$$\frac{1}{C^2} = \frac{2}{A^2 e \varepsilon_r \varepsilon_0 N_A}\left(V_{bi} - V\right) \qquad (1)$$

where C is the capacitance, A is the device area, e is the elementary charge, ε_{r} is the relative dielectric constant, ε_0 is the vacuum dielectric constant, and V is the applied bias. The V_{bi} of the control device was 0.455 V while that of the target device was 0.510 V, revealing an enhancement of carrier transport in the C_{60}-$2NH_3$-treated devices.

The performance of PSCs depends strongly on the defect state density of the perovskite film, and to quantitatively estimate the defect state density, we fitted the space charge limited current (SCLC) profile of the devices. For this purpose, hole-only devices ITO/PEDOT: PSS/perovskite (the target devices used C_{60}-$2NH_3$ modification)/P3HT/Au were prepared and *J-V* curves were obtained. We used the following formula to evaluate the trap density:

$$N_{traps} = \frac{2\varepsilon_0\varepsilon_r V_{TFL}}{ed^2} \qquad (2)$$

where N_{traps} is the trap density, V_{TFL} is the limiting voltage for filling traps, and d is the thickness of the perovskite films. As shown in Figure 4e, the V_{TFL} of the target devices decreased from 0.71 V in the control to 0.48 V, which indicated that the defect density of the C_{60}-$2NH_3$-treated perovskite was reduced, and the N_{traps} of the target devices were calculated to be reduced from 1.10×10^{15} cm^{-3} in the control to 7.43×10^{14} cm^{-3}, which were mainly attributed to the improved quality of the film supported by a reduced number of defects after the post-treatment. To quantify the change in carrier mobility in thin films, we utilized the Mott-Gurney law based on the SCLC curves:

$$\mu = \frac{8d^3 J}{9\varepsilon_0\varepsilon_r V^2} \qquad (3)$$

where J and V are the current and open voltage, respectively, in the SCLC region.[54] After calculation, as shown in Figure 4f, the electron mobility was enhanced from 3.27×10^{-3} $\mathrm{cm}^2\ \mathrm{V}^{-1}\ \mathrm{s}^{-1}$ to 4.43×10^{-3} $\mathrm{cm}^2\ \mathrm{V}^{-1}\ \mathrm{s}^{-1}$ by making use of C_{60}-$2NH_3$, which mitigated the accumulation of charge at the interface and facilitated the transfer of electrons.[55] This improvement can be simply attributed to the fact that the addition of C_{60}-$2NH_3$ reduces the defects on the perovskite surface, suppresses non-radiative recombination, improves film quality, and facilitates carrier transport. Interestingly, the grain size was not greatly affected, as it is evident by the cross-sectional SEM images in Figure S27 (Supporting Information). Finally, we prepared four films as shown in Figure S28 (Supporting Information) to measure their conductivity, and to better understand the effect of C_{60}-2NH_3 addition in the devices. Two of the films contain a layer of C_{60} for comparison purposes. The conductivity of the films after the post-treatment were all higher than those of the control films. Moreover, after evaporation of the C_{60}, the conductivity was further increased by an order of magnitude, consistent with the electron mobility results discussed above.

Regarding the operational performance between the treated and untreated devices, Figure 5a shows a substantial improvement in the average cell photovoltaic parameters of the treated devices compared to the control group. We further investigated the effects of various concentrations of C_{60}-2NH_3 on device performance, as evident in Figure S29 and Table S8 (Supporting Information). Upon analysis, the determination of the optimal post-processing concentration of C_{60}-2NH_3 was found to be 0.75 mg/ml. This concentration yielded champion devices, as depicted in Figure 5b, showcasing a V_{OC} of 0.86 V, a J_{SC} of 30.79 mA cm^{-2}, an FF of 81.84%, and a champion PCE of 21.64%. In addition, we assessed the stability of the control and target devices over ten minutes, giving rise to an SPO efficiency of 18.38% and 21.32% (Figure 5c). The devices' performance was further validated by the EQE spectra (Figure 5d), confirming a J_{SC} of 30.3 mA cm^{-2}, consistent with the values obtained from J-V measurements. Beyond efficiency, the C_{60}-2NH_3 treatment significantly improved film and device stability. As depicted in Figure S30 (Supporting Information), the target films exhibited minimal changes in absorption and surface topography even after 13 days of storage in air with high moisture levels (RH = 50-70%). In contrast, control films displayed noticeable degradation, evident in the disappearance of absorption related to mixed Sn-Pb perovskite compounds. These results confirmed that the C_{60}-2NH_3 post-treatment enhances the film's air and moisture stability, thereby helping to improve the stability of our devices. To validate this in device assembly, both control and target devices were placed in a nitrogen environment within a glove box. Apparently, the target devices retained approximately 90% of their initial efficiency after 2400 hours (Figure 5e). In comparison, the control device maintained only 90% of its initial efficiency after 600 hours. Moreover, we performed the maximum power point (MPP) tracking at around 55°C without a cooling system. As depicted in Figure S31 (Supporting Information), the control device could only retain approximately 75% of its initial efficiency after 140 hours of operation. In comparison, the target device could maintain 91% of its initial efficiency under the same conditions, affirming the effectiveness of our C_{60}-2NH_3 surface modification strategy in enhancing stability. Consequently, the introduction of C_{60}-2NH_3 significantly enhanced both the efficiency and stability of ideal-bandgap PSCs. Given its significance, we anticipate that our strategy, involving a newly developed surface passivation layer along with the first-reported 2D material featuring a C_{60} functional group, holds great potential for enhancing solar cell performance within the broader perovskite community, especially for devices using C_{60} as the electron transport layers. This approach may not only impact surface passivation but also extend to bulk perovskites, potentially leading to the formation of mixed 2D/3D perovskites in the bulk.

3. Conclusions

The motivation behind our work stemmed from the need to develop next-generation multifunctional PSC interlayer materials in single-crystal form, that would allow the study and elucidation of structure-property relationships in a concrete way. Their presence would enhance PSCs performance by improving interlayer interactions within the device, thus facilitating interlayer carrier transport.

Towards this end, by means of molecular and crystal engineering, we designed and synthesized the first member of a new family of crystalline fullerene-based metal halide semiconductors (FMHS), namely $(C_{60}\text{-}2NH_3)Pb_2I_6$. The material is a 2D semiconductor featuring a type-II band alignment, with a conduction band dominated by the $C_{60}\text{-}2NH_3$ molecule states. At the same time, a reduced dielectric contrast between the organic and the inorganic layers is also predicted as compared to conventional 2D halide perovskites, which could facilitate carrier transport. To test our hypothesis, we utilized the functionalized $C_{60}\text{-}2NH_3$ as an interlayer among the 3D perovskite light-absorbing layer and the C_{60} ETL. Our studies demonstrated that locally at the interface a thin 2D $(C_{60}\text{-}2NH_3)Pb_2I_6$ layer on top of the 3D perovskite layer can be formed. The reduced dielectric confinement within the material's sublayers and the compound's high affinity for adjacent device layers were expected to promote significant carrier transport. Indeed, $C_{60}\text{-}2NH_3$ presence had a series of positive repercussions that improved both device efficiency and stability. By utilizing a battery of characterization techniques, we identified that it suppressed PbI_2 segregation and Sn^{4+} formation, enhanced band energy alignment among the layers, promoted charged transport and extraction, and reduced the number of traps and defects. Corresponding features were translated into a champion efficiency of 21.64%, as compared to 18.87% for the non-treated device. In terms of long-term operational stability, the treated device maintained 90% of its initial efficiency, after being stored in a glove box under an N_2 environment for 2400 h. In addition, MPP tracking experiments at around 55°C without a cooling system, revealed that the target device retained 91% of its initial efficiency after 140 hours of operation. This poses a significant improvement over the control device, which maintained just 75% of its initial efficiency under the same conditions.

We expect the new family of crystalline FMHS materials to offer opportunities beyond photovoltaics, including catalysis, transistors, and supercapacitors.

4. Experimental Section

Experimental details are provided in the Supporting Information.

Corresponding Authors

spanopoulos@usf.edu
wenwenzheng@wit.edu.cn

Author Contributions

[#]W. Shen, A. Azmy, and G. Li contributed equally to this work.

Supporting Information

Supporting Information is available from the Online Library or from the author.

Accession Codes

CCDC 2306383 contains the supplementary crystallographic data for this paper. These data can be obtained free of charge via www.ccdc.cam.ac.uk/data_request/cif,orbyemailingdata_request@ccdc.cam.ac.uk, or by contacting The Cambridge Crystallographic Data Centre, 12 Union Road, Cambridge CB2 1EZ, UK; fax: +44 1223 336033.

Acknowledgements

This work was primarily supported by USF startup funds. We acknowledge support by the Key Lab of Artificial Micro-and Nano-Structures of Ministry of Education of China, Wuhan University. The authors thank the Core Facility of Wuhan University for SEM, XPS, UPS and XRD measurements. The authors also acknowledge the financial support from the National Natural Science Foundation of China (Grant Numbers: 12174290) and the Natural Science Foundation of Hubei Province, China (Grant Number: 2023AFB679) and Education Innovation Fund of Wuhan Institute of Technology (Grant Number: CX2022470). J.E., G.V., and M.K. acknowledge GENCI for the granted access to the HPC resources of TGCC under the allocations 2022-A0130907682. G.V. acknowledges funding from the ANR through the CPJ programme and the SURFIN project. J.E. acknowledges the financial support from the Institut Universitaire de France.

Conflict of Interest

The authors declare no conflict of interest.

References

[1] A. S. R. Bati, Y. L. Zhong, P. L. Burn, M. K. Nazeeruddin, P. E. Shaw, M. Batmunkh, *Commun. Mater.* **2023**, *4*, 2.

[2] aQ. Tu, I. Spanopoulos, S. Hao, C. Wolverton, M. G. Kanatzidis, G. S. Shekhawat, V. P. Dravid, *ACS Appl. Mater. Interfaces* **2018**, *10*, 22167-22173; bB. R. Sutherland, E. H. Sargent, *Nat. Photonics*

2016, *10*, 295-302.
[3] P. Wang, Y. Wu, B. Cai, Q. Ma, X. Zheng, W.-H. Zhang, *Adv. Funct. Mater.* **2019**, *29*, 1807661.
[4] D. Zhao, Y. Yu, C. Wang, W. Liao, N. Shrestha, C. R. Grice, A. J. Cimaroli, L. Guan, R. J. Ellingson, K. Zhu, X. Zhao, R.-G. Xiong, Y. Yan, *Nat. Energy* **2017**, *2*, 17018.
[5] aS. D. Stranks, G. E. Eperon, G. Grancini, C. Menelaou, M. J. P. Alcocer, T. Leijtens, L. M. Herz, A. Petrozza, H. J. Snaith, *Science* **2013**, *342*, 341-344; bQ. Dong, Y. Fang, Y. Shao, P. Mulligan, J. Qiu, L. Cao, J. Huang, *Science* **2015**, *347*, 967-970.
[6] W.-J. Yin, T. Shi, Y. Yan, *Adv. Mater.* **2014**, *26*, 4653-4658.
[7] aJ. Burschka, N. Pellet, S. J. Moon, R. Humphry-Baker, P. Gao, M. K. Nazeeruddin, M. Gratzel, *Nature* **2013**, *499*, 316-319; bI. Chung, B. Lee, J. He, R. P. Chang, M. G. Kanatzidis, *Nature* **2012**, *485*, 486-489; cW. Ke, G. Fang, J. Wan, H. Tao, Q. Liu, L. Xiong, P. Qin, J. Wang, H. Lei, G. Yang, M. Qin, X. Zhao, Y. Yan, *Nat Commun* **2015**, *6*, 6700; dH. S. Kim, C. R. Lee, J. H. Im, K. B. Lee, T. Moehl, A. Marchioro, S. J. Moon, R. Humphry-Baker, J. H. Yum, J. E. Moser, M. Gratzel, N. G. Park, *Sci Rep* **2012**, *2*, 591; eN. R. E. Laboratory*, Vol. 2023*, **2023**.
[8] W. Shockley, H. J. Queisser, *J. Appl. Phys.* **1961**, *32*, 510-519.
[9] aY. Xu, S. Xiong, S. Jiang, J. Yang, D. Li, H. Wu, X. You, Y. Zhang, Z. Ma, J. Xu, J. Tang, Y. Yao, Z. Sun, Q. Bao, *Adv. Energy Mater.* **2023**, *13*, 2203505; bF. H. Isikgor, S. Zhumagali, L. V. T. Merino, M. De Bastiani, I. McCulloch, S. De Wolf, *Nat. Rev. Mater.* **2023**, *8*, 89-108.
[10] H. J. Snaith, M. Grätzel, *Appl. Phys. Lett.* **2006**, *89*.
[11] Z. Hawash, L. K. Ono, S. R. Raga, M. V. Lee, Y. Qi, *Chem. Mater.* **2015**, *27*, 562-569.
[12] W. Song, L. Rakocevic, R. Thiruvallur Eachambadi, W. Qiu, J. P. Bastos, R. Gehlhaar, Y. Kuang, A. Hadipour, T. Aernouts, J. Poortmans, *ACS Appl. Mater. Interfaces* **2021**, *13*, 44294-44301.
[13] P. Schulz, E. Edri, S. Kirmayer, G. Hodes, D. Cahen, A. Kahn, *Energy Environ. Sci.* **2014**, *7*, 1377-1381.
[14] I. Lee, J. H. Yun, H. J. Son, T.-S. Kim, *ACS Appl. Mater. Interfaces* **2017**, *9*, 7029-7035.
[15] S. Pont, F. Foglia, A. M. Higgins, J. R. Durrant, J. T. Cabral, *Adv. Funct. Mater.* **2018**, *28*, 1802520.
[16] A. Distler, T. Sauermann, H.-J. Egelhaaf, S. Rodman, D. Waller, K.-S. Cheon, M. Lee, D. M. Guldi, *Adv. Energy Mater.* **2014**, *4*, 1300693.
[17] aR. He, W. Wang, Z. Yi, F. Lang, C. Chen, J. Luo, J. Zhu, J. Thiesbrummel, S. Shah, K. Wei, Y. Luo, C. Wang, H. Lai, H. Huang, J. Zhou, B. Zou, X. Yin, S. Ren, X. Hao, L. Wu, J. Zhang, J. Zhang, M. Stolterfoht, F. Fu, W. Tang, D. Zhao, *Nature* **2023**; bJ. Zhu, Y. Luo, R. He, C. Chen, Y. Wang, J. Luo, Z. Yi, J. Thiesbrummel, C. Wang, F. Lang, H. Lai, Y. Xu, J. Wang, Z. Zhang, W. Liang, G. Cui, S. Ren, X. Hao, H. Huang, Y. Wang, F. Yao, Q. Lin, L. Wu, J. Zhang, M. Stolterfoht, F. Fu, D. Zhao, *Nat. Energy* **2023**, *8*, 714-724.
[18] B. Li, X. Wu, H. Zhang, S. Zhang, Z. Li, D. Gao, C. Zhang, M. Chen, S. Xiao, A. K.-Y. Jen, S. Yang, Z. Zhu, *Adv. Funct. Mater.* **2022**, *32*, 2205870.
[19] W. Zhou, L. Jia, M. Chen, X. Li, Z. Su, Y. Shang, X. Jiang, X. Gao, T. Chen, M. Wang, Z. Zhu, Y. Lu, S. Yang, *Adv. Funct. Mater.* **2022**, *32*, 2201374.
[20] Z. Xing, F. Liu, S. H. Li, X. Huang, A. Fan, Q. Huang, S. Yang, *Angew Chem Int Ed Engl* **2023**, e202305357.
[21] S. You, H. Zeng, Y. Liu, B. Han, M. Li, L. Li, X. Zheng, R. Guo, L. Luo, Z. Li, C. Zhang, R. Liu, Y. Zhao, S. Zhang, Q. Peng, T. Wang, Q. Chen, F. T. Eickemeyer, B. Carlsen, S. M. Zakeeruddin, L. Mai, Y. Rong, M. Gratzel, X. Li, *Science* **2023**, *379*, 288-294.
[22] A. Fakharuddin, K.-K. Armadorou, L. P. Zorba, M. Tountas, T. Seewald, A. Soultati, P. Tsipas, E. R. Schütz, N. Tzoganakis, S. Panagiotakis, K. Yannakopoulou, A. Dimoulas, V. Psycharis, E. Kymakis, A. R. b. M. Yusoff, K. Aidinis, L. Schmidt-Mende, G. C. Vougioukalakis, M. K. Nazeeruddin, M. Vasilopoulou, *Chin. J. Chem .* **2023**, *41*, 431-442.
[23] C. Sun, P. Yang, Z. Nan, C. Tian, Y. Cai, J. Chen, F. Qi, H. Tian, L. Xie, L. Meng, Z. Wei, *Adv. Mater.* **2023**, *35*, 2205603.
[24] Y. Jiang, J. Wang, H. Zai, D. Ni, J. Wang, P. Xue, N. Li, B. Jia, H. Lu, Y. Zhang, F. Wang, Z. Guo, Z. Bi, H. Xie, Q. Wang, W. Ma, Y. Tu, H. Zhou, X. Zhan, *J. Am. Chem. Soc.* **2022**, *144*, 5400-5410.
[25] J. Yin, X. Shi, L. Wang, H. Yan, S. Chen, *Angew. Chem. Int. Ed.* **2022**, *61*, e202210610.
[26] aY. Kawabata, M. Yoshizawa-Fujita, Y. Takeoka, M. Rikukawa, *Synth. Met.* **2009**, *159*, 776-779; bK.

Kikuchi, Y. Takeoka, M. Rikukawa, K. Sanui, *Colloids and Surfaces A: Physicochem. Eng. Aspects* **2005**, *257-258*, 199-202; cB. Choi, J. Yu, D. W. Paley, M. T. Trinh, M. V. Paley, J. M. Karch, A. C. Crowther, C.-H. Lee, R. A. Lalancette, X. Zhu, P. Kim, M. L. Steigerwald, C. Nuckolls, X. Roy, *Nano Lett.* **2016**, *16*, 1445-1449; dD. E. Williams, E. A. Dolgopolova, D. C. Godfrey, E. D. Ermolaeva, P. J. Pellechia, A. B. Greytak, M. D. Smith, S. M. Avdoshenko, A. A. Popov, N. B. Shustova, *Angew. Chem. Int. Ed.* **2016**, *55*, 9070-9074; eD. B. Straus, R. J. Cava, *J. Am. Chem. Soc.* **2020**, *142*, 13155-13161.

[27] J. V. Passarelli, D. J. Fairfield, N. A. Sather, M. P. Hendricks, H. Sai, C. L. Stern, S. I. Stupp, *J. Am. Chem. Soc.* **2018**, *140*, 7313-7323.

[28] H. W. Kroto, J. R. Heath, S. C. O'Brien, R. F. Curl, R. E. Smalley, *Nature* **1985**, *318*, 162-163.

[29] N. Mercier, *Angew. Chem. Int. Ed.* **2019**, *58*, 17912-17917.

[30] C. Katan, N. Mercier, J. Even, *Chem. Rev.* **2019**, *119*, 3140-3192.

[31] A. R. Puente Santiago, O. Fernandez-Delgado, A. Gomez, M. A. Ahsan, L. Echegoyen, *Angew. Chem. Int. Ed.* **2021**, *60*, 122-141.

[32] C. G. Bischak, L. Q. Flagg, K. Yan, C.-Z. Li, D. S. Ginger, *ACS Appl. Mater. Interfaces* **2019**, *11*, 28138-28144.

[33] Z. Peng, Y. Hu, J. Wang, S. Liu, C. Li, Q. Jiang, J. Lu, X. Zeng, P. Peng, F.-F. Li, *Adv. Energy Mater.* **2019**, *9*, 1802928.

[34] C. F. Richardson, D. I. Schuster, S. R. Wilson, *Org. Lett.* **2000**, *2*, 1011-1014.

[35] aN. Chronakis, U. Hartnagel, M. Braun, A. Hirsch, *Chem. Commun.* **2007**, 607-609; bX. Camps, A. Hirsch, *J. Chem. Soc., Perkin Trans. 1* **1997**, 1595-1596; cC. Bingel, *Chem. Ber.* **1993**, *126*, 1957-1959.

[36] aJ. A. Alonso, M. J. Martínez-Lope, M. T. Casais, M. T. Fernández-Díaz, *Inorg. Chem.* **2000**, *39*, 917-923; bK.-z. Du, Q. Tu, X. Zhang, Q. Han, J. Liu, S. Zauscher, D. B. Mitzi, *Inorg. Chem.* **2017**, *56*, 9291-9302; cK. Robinson, G. V. Gibbs, P. H. Ribbe, *Science* **1971**, *172*, 567-570.

[37] D. G. Billing, A. Lemmerer, *Acta Crystallogr. Sect. B* **2007**, *63*, 735-747.

[38] D. G. Billing, A. Lemmerer, *New J. Chem.* **2008**, *32*, 1736-1746.

[39] W. I. F. David, R. M. Ibberson, J. C. Matthewman, K. Prassides, T. J. S. Dennis, J. P. Hare, H. W. Kroto, R. Taylor, D. R. M. Walton, *Nature* **1991**, *353*, 147-149.

[40] P. Trucano, R. Chen, *Nature* **1975**, *258*, 136-137.

[41] L. Pedesseau, D. Sapori, B. Traore, R. Robles, H.-H. Fang, M. A. Loi, H. Tsai, W. Nie, J.-C. Blancon, A. Neukirch, S. Tretiak, A. D. Mohite, C. Katan, J. Even, M. Kepenekian, *ACS Nano* **2016**, *10*, 9776-9786.

[42] B. Traore, L. Pedesseau, L. Assam, X. Che, J.-C. Blancon, H. Tsai, W. Nie, C. C. Stoumpos, M. G. Kanatzidis, S. Tretiak, A. D. Mohite, J. Even, M. Kepenekian, C. Katan, *ACS Nano* **2018**, *12*, 3321-3332.

[43] Z. Yang, X. Cao, G. Niu, Y. Wang, Y. Dong, S. Cao, W. Liu, X. Wang, Y. Liu, J. Wang, *Chem. Eng. J.* **2023**, *464*, 142720.

[44] aJ. Liang, X. Hu, C. Wang, C. Liang, C. Chen, M. Xiao, J. Li, C. Tao, G. Xing, R. Yu, W. Ke, G. Fang, *Joule* **2022**, *6*, 816-833; bG. Li, Y. Hu, M. Li, Y. Tang, Z. Zhang, A. Musiienko, Q. Cao, F. Akhundova, J. Li, K. Prashanthan, F. Yang, P. Janasik, A. N. S. Appiah, S. Trofimov, N. Livakas, S. Zuo, L. Wu, L. Wang, Y. Yang, B. Agyei-Tuffour, R. W. MacQueen, B. Naydenov, T. Unold, E. Unger, E. Aktas, S. Eigler, A. Abate, *Angew. Chem. Int. Ed.* **2023**, *62*, e202307395.

[45] J. Luo, R. He, H. Lai, C. Chen, J. Zhu, Y. Xu, F. Yao, T. Ma, Y. Luo, Z. Yi, Y. Jiang, Z. Gao, J. Wang, W. Wang, H. Huang, Y. Wang, S. Ren, Q. Lin, C. Wang, F. Fu, D. Zhao, *Adv Mater* **2023**, *35*, e2300352.

[46] aS. Gupta, T. Bendikov, G. Hodes, D. Cahen, *ACS Energy Letters* **2016**, *1*, 1028-1033; bM. H. Kumar, S. Dharani, W. L. Leong, P. P. Boix, R. R. Prabhakar, T. Baikie, C. Shi, H. Ding, R. Ramesh, M. Asta, M. Graetzel, S. G. Mhaisalkar, N. Mathews, *Adv Mater* **2014**, *26*, 7122-7127.

[47] aR. Lin, Y. Wang, Q. Lu, B. Tang, J. Li, H. Gao, Y. Gao, H. Li, C. Ding, J. Wen, P. Wu, C. Liu, S. Zhao, K. Xiao, Z. Liu, C. Ma, Y. Deng, L. Li, F. Fan, H. Tan, *Nature* **2023**, *620*, 994-1000; bX. Sun, Z. Li, X. Yu, X. Wu, C. Zhong, D. Liu, D. Lei, A. K. Jen, Z. Li, Z. Zhu, *Angew Chem Int Ed Engl* **2021**, *60*, 7227-7233; cX. Yu, Z. Li, X. Sun, C. Zhong, Z. Zhu, Z. a. Li, A. K. Y. Jen, *Nano Energy* **2021**, *82*; dY. Wu, X. Yang, W. Chen, Y. Yue, M. Cai, F. Xie, E. Bi, A. Islam, L. Han, *Nat. Energy* **2016**, *1*, 16148.

[48] L. Huang, H. Cui, W. Zhang, D. Pu, G. Zeng, Y. Liu, S. Zhou, C. Wang, J. Zhou, C. Wang, H. Guan, W. Shen, G. Li, T. Wang, W. Zheng, G. Fang, W. Ke, *Adv Mater* **2023**, e2301125.

[49] D. Meggiolaro, D. Ricciarelli, A. A. Alasmari, F. A. S. Alasmary, F. De Angelis, *J Phys Chem Lett* **2020**, *11*, 3546-3556.

[50] aV. M. Le Corre, E. A. Duijnstee, O. El Tambouli, J. M. Ball, H. J. Snaith, J. Lim, L. J. A. Koster, *ACS Energy Lett* **2021**, *6*, 1087-1094; bY. Zhong, G. Liu, Y. Su, W. Sheng, L. Gong, J. Zhang, L. Tan, Y. Chen, *Angew Chem Int Ed Engl* **2022**, *61*, e202114588; cX. Zhang, D. Zhang, Y. Zhou, Y. Du, J. Jin, Z. Zhu, Z. Wang, X. Cui, J. Li, S. Wu, J. Zhang, Q. Tai, *Adv. Funct. Mater.* **2022**, *32*, 2205478.

[51] aS. Wu, Z. Li, J. Zhang, T. Liu, Z. Zhu, A. K. Jen, *Chem Commun (Camb)* **2019**, *55*, 4315-4318; bX. Wu, F. Qi, F. Li, X. Deng, Z. Li, S. Wu, T. Liu, Y. Liu, J. Zhang, Z. Zhu, *Energy Environ. Mater.* **2021**, *4*, 95-102.

[52] aC. Wang, Y. Zhao, T. Ma, Y. An, R. He, J. Zhu, C. Chen, S. Ren, F. Fu, D. Zhao, X. Li, *Nat. Energy* **2022**, *7*, 744-753; bW. Pan, H. Wu, J. Luo, Z. Deng, C. Ge, C. Chen, X. Jiang, W.-J. Yin, G. Niu, L. Zhu, L. Yin, Y. Zhou, Q. Xie, X. Ke, M. Sui, J. Tang, *Nat. Photonics* **2017**, *11*, 726-732.

[53] A. Rajagopal, P.-W. Liang, C.-C. Chueh, Z. Yang, A. K. Y. Jen, *ACS Energy Lett.* **2017**, *2*, 2531-2539.

[54] S. Wang, Y. Liu, C. Liu, W. Shao, C. Wang, M. Xiao, G. Chen, Z. Yu, C. Tao, W. Ke, G. Fang, *Laser Photonics Rev.* **2023**, *17*, 2200871.

[55] W. Ding, H. Liu, S. Zhang, D. Qiu, X. Li, S. Wang, *Adv. Funct. Mater.* **2022**, *32*, 2105164.

Figures

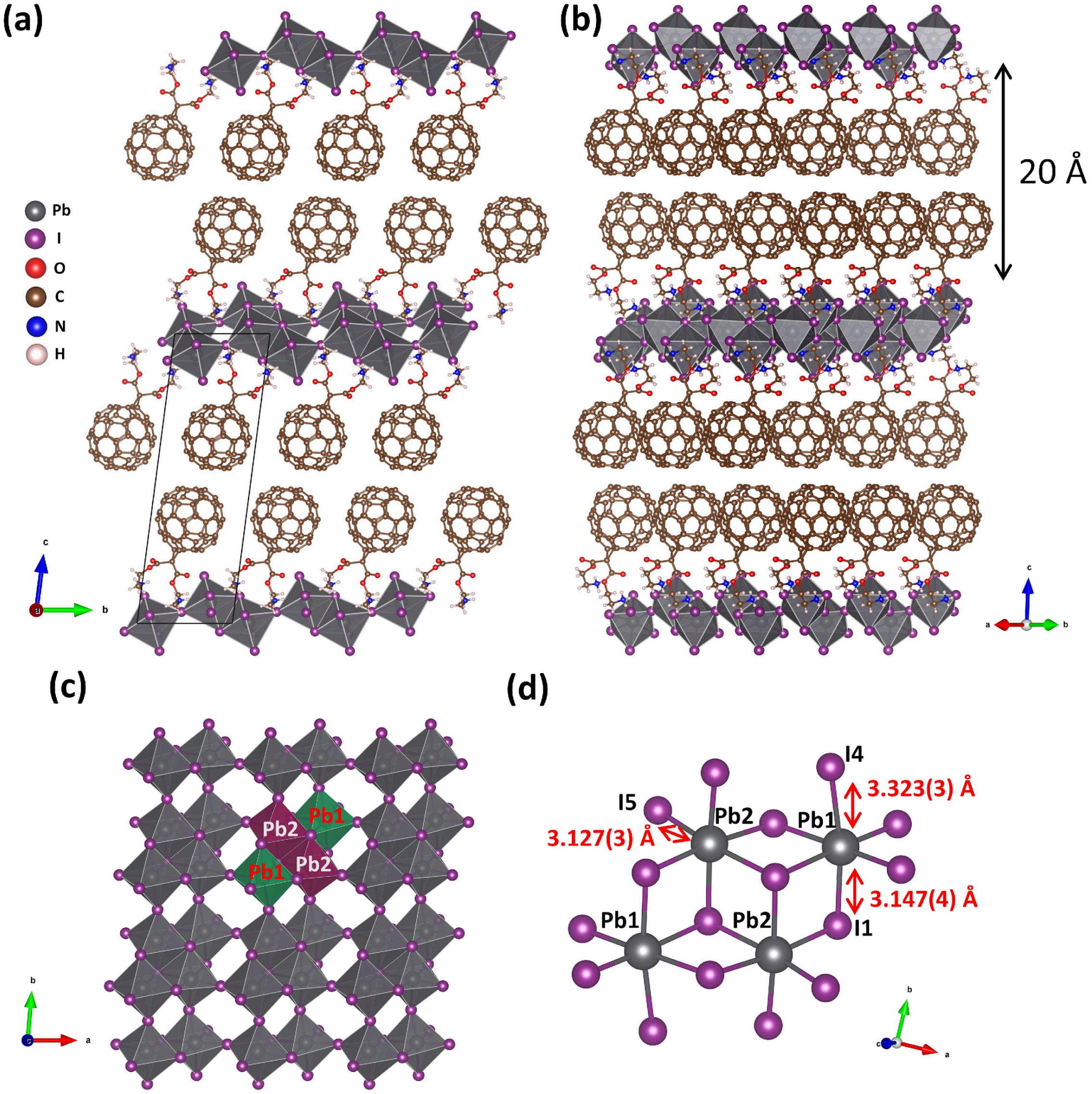

Figure 1. (a) Part of the layered structure of (C_{60}-2NH_3)Pb_2I_6 viewing along the a-axis and (b) the (110) plane. Adjacent inorganic layers lay at a distance of 20 Å. (c) A single inorganic layer consisting of corner-sharing $[Pb_4I_{16}]^{8-}$ tetramers. (d) Structural configuration of the $[Pb_4I_{16}]^{8-}$ tetramers presenting the octahedral connectivity and representative Pb-I bond lengths.

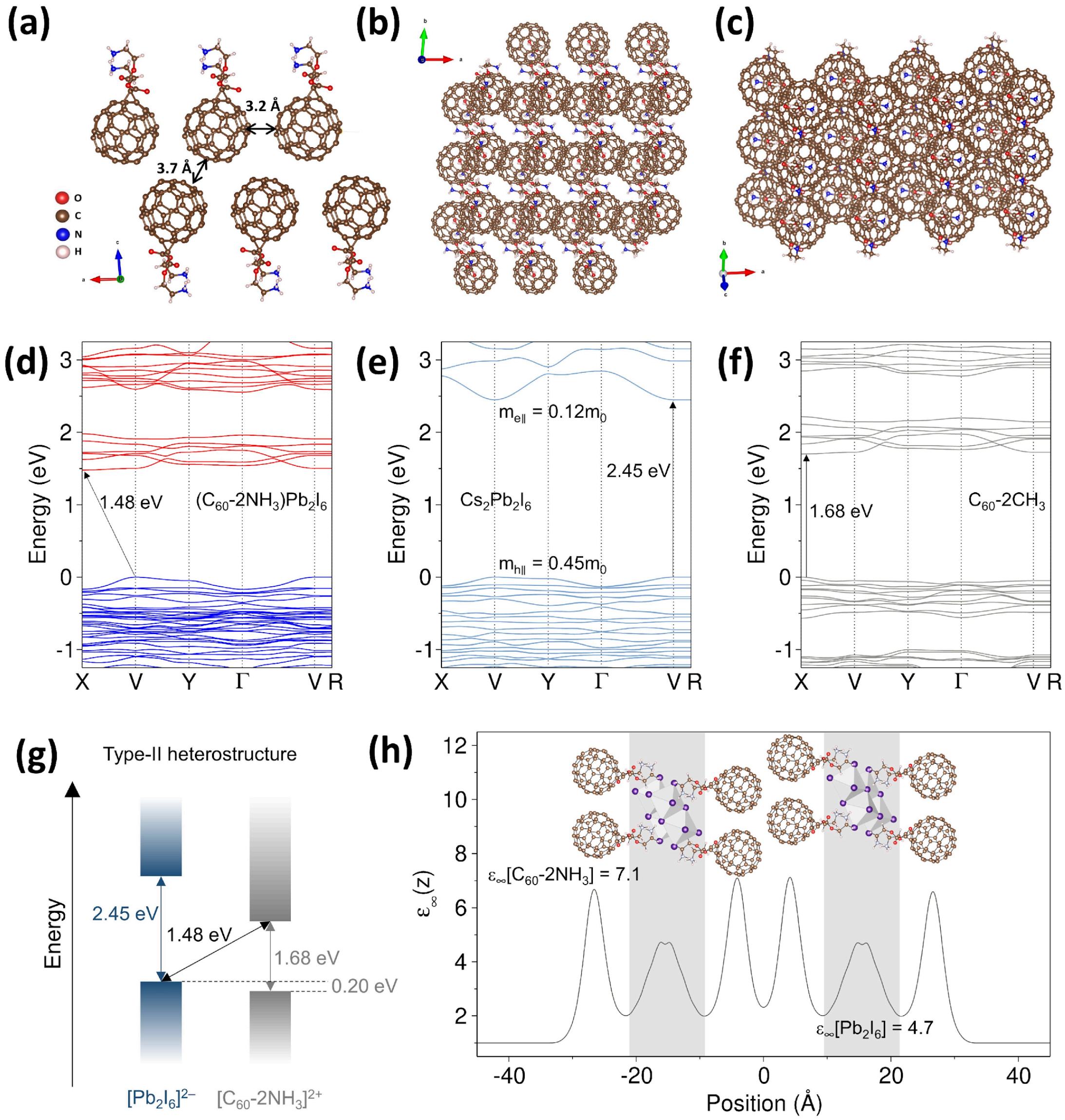

Figure 2. (a) Part of the organic sublayers of $(C_{60}\text{-}2NH_3)Pb_2I_6$ viewing along the b-axis and (b) c-axis. $C_{60}\text{-}2NH_3$ molecules feature an anti-configuration laying at a distance of 3.2 Å in-plane, and at 3.7 Å out-of-plane, indicative of the extensive π-π interactions. (c) The packing configuration of $C_{60}\text{-}2NH_3$ resembles the packing of crystalline C_{60}. (d) Calculated band structure of $(C_{60}\text{-}2NH_3)Pb_2I_6$ using HSE06 correction for the band gaps (see Supporting Information). (e) Band structure of the $[Pb_2I_6]^{2-}$ moiety where molecular cations are emulated by Cs^+ atoms. (f) Band structure of the organic layer with $-NH_3^+$ group substituted by $-CH_3$ to ensure charge neutrality in the system. (g) Band alignment between the inorganic and organic layers of $(C_{60}\text{-}2NH_3)Pb_2I_6$ showing a type-II alignment. (h) High-frequency dielectric profile along the stacking axis exhibiting a smaller dielectric contrast than for classical layered halide perovskites.

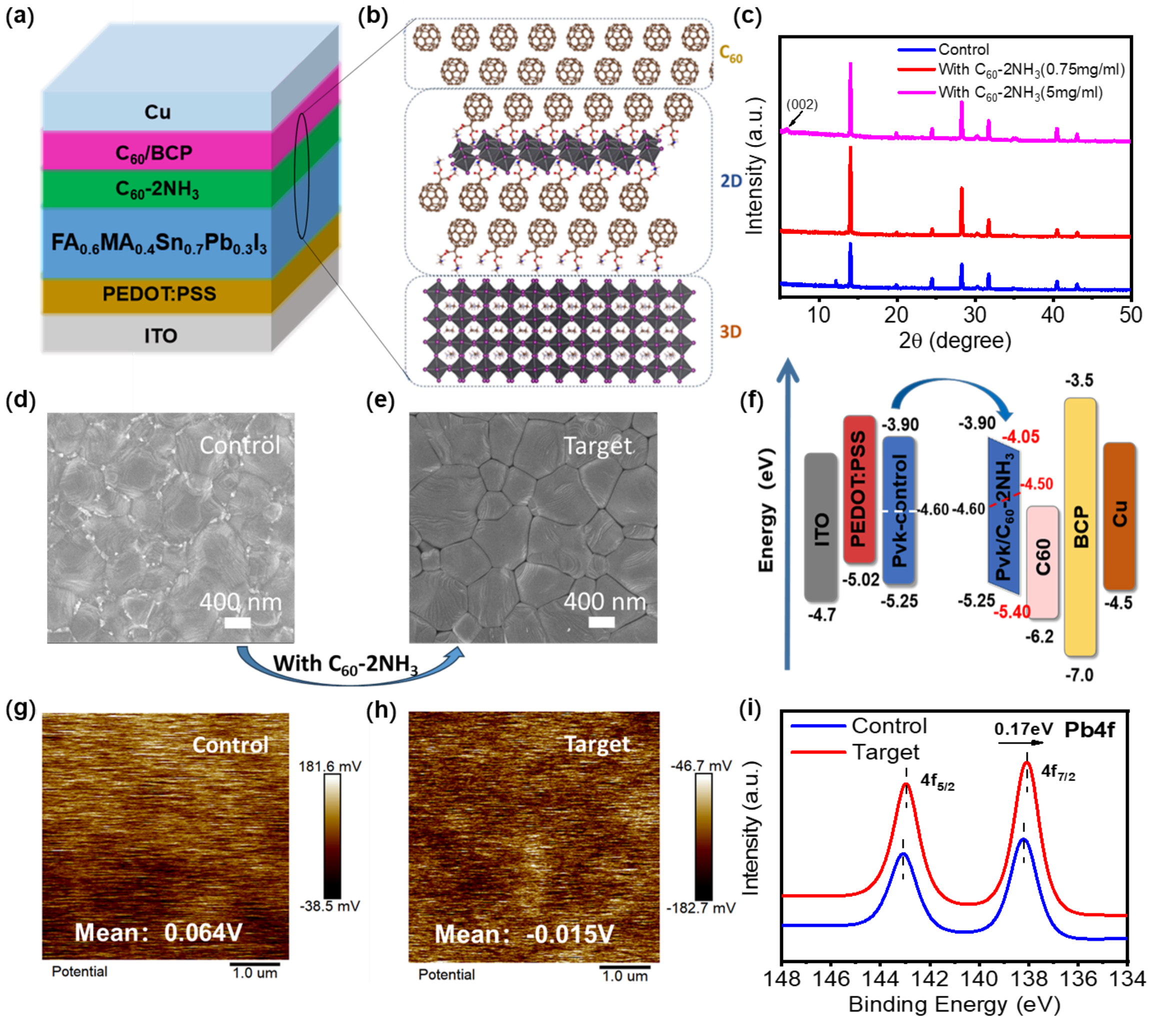

Figure 3. (a) Device architecture of the prepared $FA_{0.6}MA_{0.4}Pb_{0.7}Sn_{0.3}I_3$ perovskite solar cells. (b) Schematic representation of the surface passivation mechanism of Sn-Pb perovskite thin film grains introduced with C_{60}-2NH_3. There is reduced dielectric confinement of the generated carriers in (C_{60}-2NH_3)Pb_2I_6, while the 2D material features high affinity for both the ETL (π-π interactions) and light absorbing layer (electrostatic interactions). Therefore, the presence of a thin layer of (C_{60}-2NH_3)Pb_2I_6 can act as a passivating layer facilitating carrier transport between the 3D perovskite and the ETL. (c) XRD patterns of Sn-Pb perovskite films without and with C60-2NH3 post-treatment at different concentrations. SEM images of control (d) perovskite films and C_{60}-2NH_3 post-treated (e) perovskite films. (f) Schematic band energy levels change of Sn-Pb ideal-bandgap PSCs with and without C_{60}-2NH_3 post-treatment. KPFM images of Sn-Pb perovskite films without (g) and with C_{60}-2NH_3 (h) post-treatment. (i) XPS spectra of Pb 4f for Sn-Pb perovskite films with and without C_{60}-2NH_3 post-treatment.

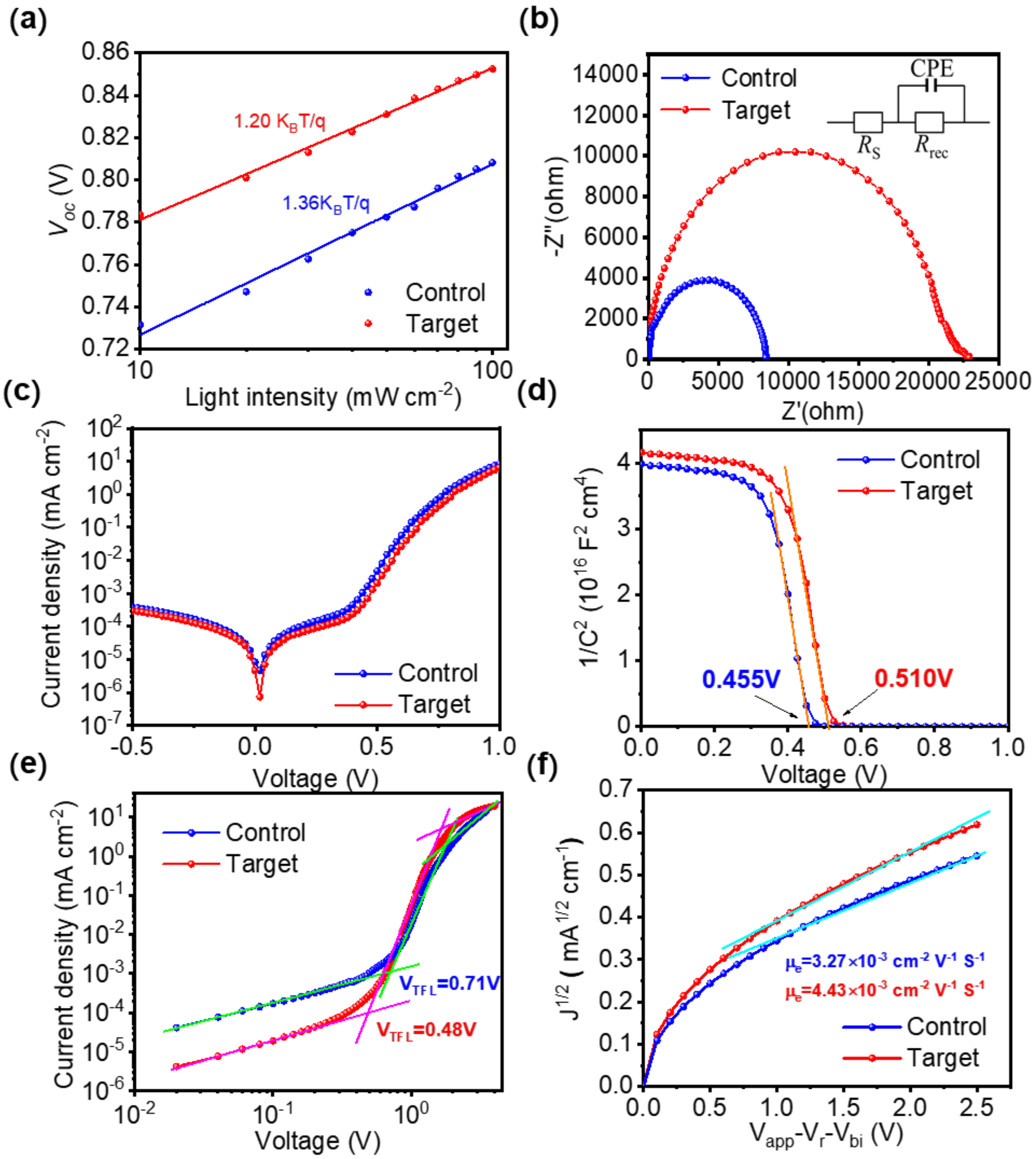

Figure 4. (a) Light intensity-dependent V_{OC} changes and slope of the linear fit. (b) Nyquist plots of control and target devices at 0.5 V in the dark. (c) Dark *J-V* curves of PSCs in control and target devices. (d) Mott-Schottky curves of PSCs with and without C_{60}-2NH_3 post-treatment. (e) Dark *J-V* responses of single-cavity devices of perovskite films with and without C_{60}-2NH_3 post-treatment (f) Electron mobility of perovskite films with and without C_{60}-2NH_3 post-treatment using space charge-limited current (SCLC).

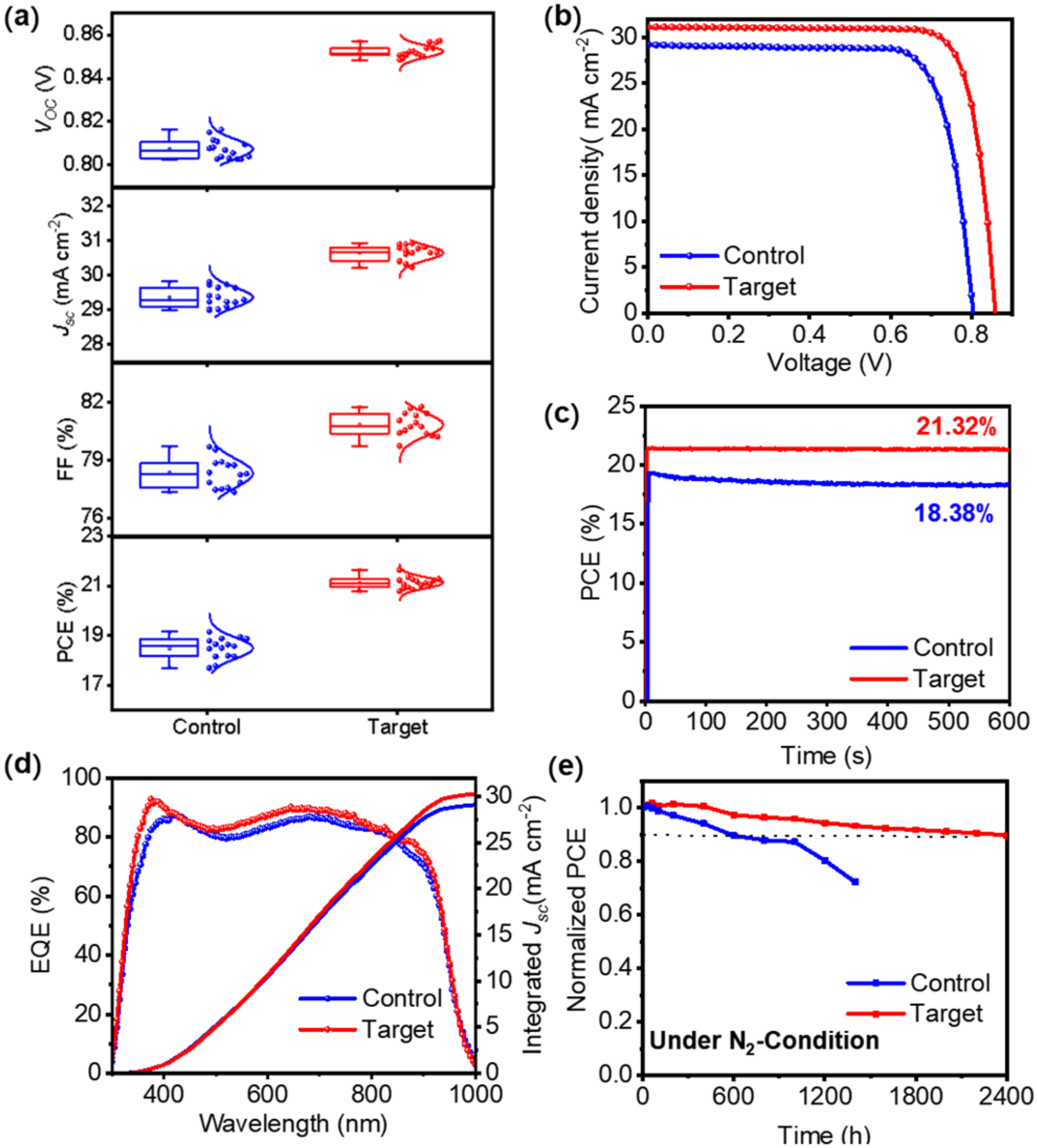

Figure 5. (a) Comparison of various photovoltaic parameters between control and target PSCs. (b) *J-V* curves of control and champion PSCs. (c) SPO efficiency of control and target PSCs. (d) EQE spectrum of control and target PSCs. (e) Normalized PCE decay curves for unencapsulated devices stored in an N_2-filled glove box.

TOC

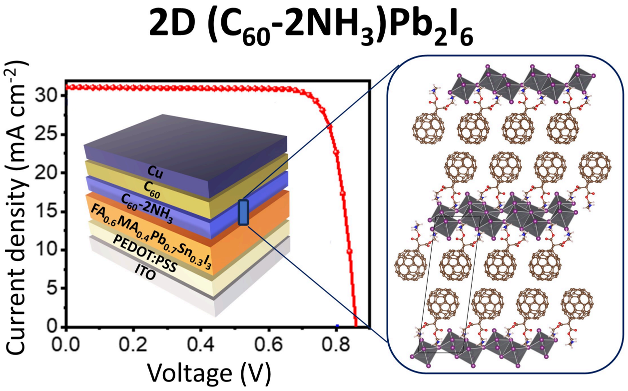

TOC narrative

The study reports the synthesis of the first crystalline fullerene-based metal halide semiconductor, namely $(C_{60}\text{-}2NH_3)Pb_2I_6$. Utilization of the $C_{60}\text{-}2NH_3I_2$ adducts as an interfacial layer in mixed Pb-Sn perovskite solar cells substantially improved both carrier transport and device stability. This work sets the foundation for the development of a new family of multifunctional materials, namely Fullerene Metal Halide Semiconductors (FMHS).